ELSEVIER

Relationship Between Differences in Silica Fume Additives and Fine-Scale Microstructural Evolution in Cement Based Materials

Andrew J. Allen* and Richard A. Livingston†

*Materials Science and Engineering Laboratory, National Institute of Standards and Technology, Gaithersburg, Maryland, USA; and †Exploratory Research, Federal Highway Administration, McLean, Virginia, USA

The effects on the microstructural development of adding silica fume to cements and concretes during cement hydration have been studied using small-angle neutron scattering and ultrasmall-angle X-ray scattering. A previously developed fractal based microstructural model has been applied to extract representative microstructural parameters from the small-angle scattering data. A link has been established between the existence of coarse or agglomerated particles in the silica fume particle size distribution and possible deleterious microstructural evolution during cement hydration. ADVANCED CEMENT BASED MATERIALS 1998, 8, 118–131. *Published by Elsevier Science Ltd.*

KEY WORDS: Cement paste, Silica fume, Microstructure, Small-angle scattering

Supplementary cementitious materials like silica fume (SF), added to a Portland cement (PC) mix, react with calcium ions in the pore solution [1] to enhance the production of calcium-silicate-hydrate gel (C-S-H) and also modify the microstructure in other ways. These modifications counter deterioration processes such as alkali-aggregate reactions or chloride penetration and, hence, improve the long-term durability of concretes into which the cement is incorporated. Whereas a suitable SF usually is distinguished by a high total specific surface area (30–50 × 10^3 m^2 kg^{-1}), the microstructural complexity of hydrating cements and concretes suggests that the detailed fume morphology, over the whole range of particle sizes, is significant in determining the fume activity. The proper use of SF requires a better understanding of its variability [2,3] as a byproduct of silicon and silicon steel manufacture. The objective of this research is to investigate how this influences the subsequent microstructural evolution during cement or concrete hydration, and how cementitious microstructures, over the whole length-scale range, can be related to the basic mechanisms governing concrete performance [4].

Whereas the strength and durability of concretes are critically dependent on their microstructures [5,6], methods for fully quantifying the characteristic microstructures representative of undisturbed concrete morphologies have not been available. The need for such methods becomes more important as the variety of materials added to concretes increases. Traditional methods for the microstructural characterization of concretes include desorption studies, mercury intrusion porosimetry, and scanning electron microscopy (SEM). Unfortunately, these methods have had limited success [7–9], because they cannot access the very fine length-scales (1 to 100 nm) that define critical aspects of the microstructure, the methods themselves create changes in the microstructure, or they require simplistic models regarding pore shape and morphology [7]. In contrast, small-angle scattering (SAS) of neutrons (SANS) or X-rays (SAXS) is most effective in this size range, is nondestructive, and is amenable to a range of model assumptions regarding pore shapes and morphologies [8–17]. Because SAS requires no destructive drying pretreatments and does not modify the microstructure itself, it can be used repeatedly in the real-time characterization of the microstructural evolution during cement hydration. SANS can be used to probe a sample volume several millimeters in diameter and ≈1 mm thick, enough to probe the undisturbed, statistically representative microstructures in cements. The technique complements methods such as transmission electron microscopy (TEM) [15], which gives a detailed but highly localized picture of the microstructure.

Address correspondence to: Dr. Andrew J. Allen, Materials Science and Engineering Laboratory, National Institute of Standards and Technology, Ceramics Division, Building 223, Room A163, Gaithersburg, Maryland 20899.

Received October 27, 1997; Accepted March 12, 1998.

Published by Elsevier Science Ltd.
655 Avenue of the Americas, New York, NY 10010

ISSN 1065-7355/98/$00.00
PII S1065-7355(98)00015-7

It has been demonstrated [15–22] that the analysis of SAS data yields several parameters, including particle size, shape, surface area, and fractal exponents, which can provide a concise, quantitative description of the microstructure. The assumption of approximately fractal microstructures over appropriate scale-ranges forms the basis of a robust mathematical representation for a variety of disordered porous morphologies, provided the data extend over a great enough high-resolution angular range to encompass the SAS associated with all significant length-scales. Other experimental requirements are that the sample thickness must be sufficiently small to give negligible multiple scattering (for example, cement samples should be no more than 1 to 2 mm thick for SANS), and that the data must be absolutely calibrated so that the relative strengths of the SAS arising in different parts of the microstructure can be assessed properly.

Previous SANS studies on hydrating cement systems have shown that modifications in the microstructural evolution can be associated with the addition of SF, pulverized fly ash, or blast furnace slag [12,15–17,20]. The present research applies SAS to the microstructural characterization of different SF additives used at water/cement (w/c) ratios typical of high performance concretes (HPC). However, in order to avoid compounding effects, the water reducer and superplasticizer admixtures usually present in HPC were not included. The microstructural evolution during hydration in 0.4 w/c PC, and in different SF/PC blends at 0.4 water-to-solid (w/s) weight ratios, have been studied by SANS. These data have been related to SAXS and SANS studies of the respective SF particle size distributions, and to previous SANS results for the early real-time hydration of a cement containing one such fume [20].

Basic Principles and Microstructural Model

In SAS studies [23], a small component of the incident beam is scattered out of the straight-through beam direction by inhomogeneities in the sample microstructure. In hydrating cement systems, the SAS component arises primarily [15] from the interface between the C-S-H gel and the cement pore water. In SF slurries, the scattering interface occurs between the silica and the slurry medium (also water).

Because there generally are no preferred orientations in cement or fume microstructures, the scattering is circularly symmetric and can be circularly averaged about the incident beam direction. Thus, the aim of the SAS data reduction is to obtain the absolute-calibrated scattered intensity or scattering cross-section, $d\Sigma/d\Omega$, as a function of the magnitude, Q, of the scattering vector, **Q**. ($Q = (4\pi/\lambda)\sin\theta$, where 2θ is the scattering angle and λ is the neutron or X-ray wavelength.) In this case, $d\Sigma/d\Omega$ is the probability rate, per unit incident neutron flux (also a rate) and per unit sample volume, of scattering into unit solid angle, Ω, about any one direction defined by a given value of Q (or 2θ). Note that $d\Sigma/d\Omega$ is a material property depending only on the microstructure and nature of the scattering radiation, not on the details of the SAS experiment.

For a given microstructure, the strength of the SAS (magnitude of $d\Sigma/d\Omega$) is proportional to the scattering contrast across the interfaces that define the scattering features. Although the hydrated cements were studied under saturated conditions, the C-S-H gel formula assumed here is that proposed [24] for cements equilibrated with 11% relative humidity: $(CaO)_{1.7}\cdot(SiO_2)\cdot(H_2O)_{2.1}$, or $C_{1.7}SH_{2.1}$ in cement notation, with a skeletal density of 2.18×10^3 kg m^{-3}, and a SANS contrast, $|\Delta\rho|^2$, between gel and pore water [25], of 6.78×10^{28} m^{-4}. This value differs slightly from that used in earlier work [15–22], but is justified by some recent SANS calibration studies [26] that establish the above formula and density as giving a better scattering contrast than either that used previously, or that for a proposed $C_{1.7}SH_{4.0}$ gel formula in saturated cement systems [24]. However, the last formula includes all of the so-called gel-pore water, and, thus, it is not surprising that some 1.9 of the 4.0 water molecules per $C_{1.7}SH_{4.0}$ formula-unit are "seen" by neutrons or X-rays as part of the pore fluid, rather than as part of the solid C-S-H phase.

In the case of the SF slurries, the scattering contrast for SiO_2 (assumed skeletal density 2.32×10^3 kg m^{-3}) in water is 16.32×10^{28} m^{-4} for SANS, and 80.82×10^{28} m^{-4} for SAXS. For comparison purposes, the SAXS data were normalized to the SANS data with an empirical normalization factor that was found to be close to the 0.2 predicted simply from the ratio of the SANS and SAXS contrasts.

Whereas some previous SANS and SAXS studies have focused on specific microstructural features [8–12, 27–30], other SANS and SAXS studies [13–17,20-22,31–38], together with porosimetry, TEM [39], and SEM and stereology [40], have indicated the presence of disordered heterogeneous porous microstructures over various length-scales. This is a defining characteristic of an approximately scale-invariant or fractal solid/pore morphology [41].

Previous SANS studies by the present authors [13–17,20–22] have revealed a mass- or volume-fractal microstructure with a volume-fractal scaling exponent $D_V = 2.5$ to 2.7. Emergence of this structure correlates approximately with the main thermal peak in the heat output of the hydration reactions, as measured by thermal calorimetry, and was associated with the development of the major C-S-H gel "outer-product," or "groundmass" phase, in the open spaces between the original clinker grains. This volume-fractal phase is characterized, using SANS, by a high surface area per unit volume of up to $\sim 200 \times 10^6$ m^{-1} (200 m^2 cm^{-3}). It also has a fundamental building block or globule size of ~5 nm, which does not seem to vary with moderate hydration times or between cement blends. Finally, the correlation length ξ_v, which defines the average upper-limit length-scale for the volume-fractal microstructure, increases from 5 to 10 nm up to 100 to 200 nm (depending on the cement mix) as hydration proceeds. These parameters are consistent with a physical model of ~ 5-nm-diameter colloidal particles of C-S-H, aggregating into clusters that grow to 100 to 200 nm in size before coalescing into one other. The sample volume fraction of what we assume to be the C-S-H outer-product phase ϕ_{CSH} was also deduced, and it too correlates with the hydration reaction heat output, at least for the first 24 hours of hydration.

At slightly later times, at smaller Q values, and hence at larger length-scales, a second type of fractal structure develops in hydrating PC systems: a surface-fractal microstructure [15–17,20–22]. The apparent surface-fractal scaling exponent D_s is usually in the range from 2.5 to 2.8, depending on cement mix and age, although it may be as low as 2.3 in SF/PC blends. The surface-fractal component has been associated with the roughening of the cement clinker grain surfaces by a layer of C-S-H outer-product. Because the surface-fractal minimum length-scale overlaps the volume-fractal length-scale range, it is more difficult to extract the surface-fractal microstructure parameters than for the volume-fractal component. Also, the average upper-limit length-scale ξ_s, possibly related to the cement clinker grain dimensions, is frequently several hundred nanometers and exceeds the practical size range of SANS instruments.

Fortunately, given the above general description, the same minimum structural scale-length should apply for the surface-fractal C-S-H gel component as for the volume-fractal C-S-H gel component. The volume-fractal minimum scale-length is the correlation-hole radius R_C, which is the minimum center-to-center distance between gel globules (the globule diameter for perfectly spherical globules). Because this and the surface-fractal scattered intensities and power laws are directly measurable, the total (rough) surface area in the surface-fractal component S_{sf} can be determined by extrapolating the surface-fractal scaling down to dimensions of order R_C using the parameters ξ_s, and S_o, as described below. The parameter S_o is the "smooth" surface of the surface-fractal microstructure, obtained by ignoring all surface roughness on length-scales smaller than ξ_s.

Microscopic stereology of fracture surfaces [40] has revealed another volume-fractal microstructure component in the coarser (1 to 10 μm) pore/grain morphology, but this is the result of different mechanisms that are not relevant here. Figure 1 shows schematically the heterogeneous cement microstructure assumed to be responsible for the observed SAS from hydrating cement systems. Figure 2 shows how the microstructural components of interest in SAS studies appear in the SANS data as plotted as $Q^4 d\Sigma/d\Omega$ versus Q on a log-log scale. Such plots are useful for revealing clearly the microstructural variations that occur during cement hydration.

For the purpose of modeling, the C-S-H gel is assumed to consist of ~5-nm-diameter globular building blocks. The assumption of solid globules as the representative building blocks [13–22], rather than the planar or foil-like C-S-H structures sometimes seen in TEM studies [39], is justified by the need to include the scattering from such individual features when modeling the observed SANS data, and by the absence in the scattering of the main hallmark of foil-like features: a Q^{-2} scattering power law. The existence of ~5-nm features within the gel is supported by some TEM studies [39], by independent SANS studies [31], by the application of thermodynamic modeling in nitrogen desorption studies [6], and by recent selected-area electron diffraction TEM studies [42].

Rather than spheres of radius R_o, it is mathematically convenient to assume the building-block globules to be spheroidal in shape, i.e., with a radius βR_o along one axis, where β is an aspect ratio close to unity. This leads to the well-known "single-particle" scattering form factor, $F^2(Q)$, derived for spheroids by Roess and Shull [43]. The functional model is then given by:

$$\begin{aligned}\frac{d\Sigma}{d\Omega} = \phi_{CSH} V_p |\Delta\rho|^2 \Bigg\{ & \frac{\eta R_C^3}{\beta R_o^3}\left(\frac{\xi_v}{R_C}\right)^{D_v} \\ & \times \frac{\sin[(D_v - 1)\arctan(Q\xi_v)]}{(D_v - 1)Q\xi_v[1 + (Q\xi_v)^2]^{(D_v-1)/2}} \\ & + (1-\eta)^2 \Bigg\} F^2(Q) \\ & + \frac{\pi\xi_S^4 |\Delta\rho|^2 S_o \Gamma(5 - D_S)\sin[(3-D_S)\arctan(Q\xi_S)]}{[1 + (Q\xi_S)^2]^{(5-D_s)/2} Q\xi_S} \\ & + \text{BACKGROUND} \end{aligned} \tag{1}$$

The first term within the large bracket gives both the volume-fractal scattering (where $d\Sigma/d\Omega \sim Q^{-D_v}$ for $QR_C \ll 1 \ll Q\xi_v$) and the single-globule scattering (where $V_p = 4\beta\pi R_o{}^3/3$, and the contrast is softened by the local packing fraction, η). The second term gives the surface-fractal scattering (where $d\Sigma/d\Omega \sim Q^{-(6 - D_s)}$ for $Q\xi_v \ll 1 \ll Q\xi_s$, and $\Gamma\{x\}$ is the Gamma function). The

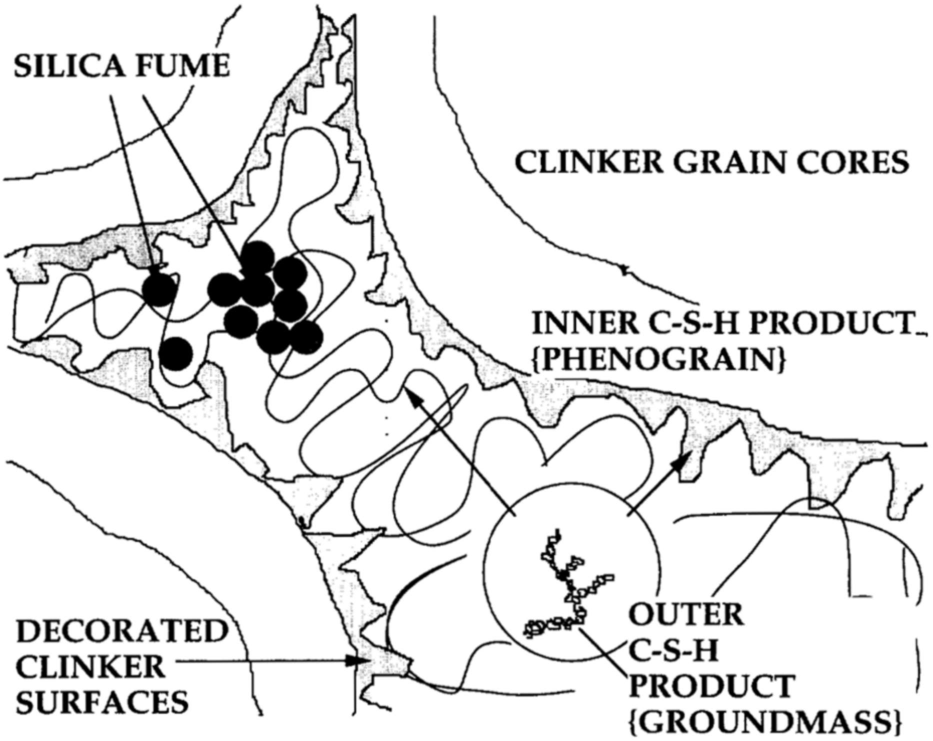

FIGURE 1. Microstructural model schematic. Outer C-S-H product between grains forms the volume-fractal phase. Decoration of clinker grains by C-S-H forms the surface-fractal phase. The influence of the silica fume morphology is discussed in the text.

BACKGROUND term allows for adjustments to be made in the incoherent flat-background scattering subtraction, significant in SANS studies of hydrogeneous systems such as hydrating cements.

Many of the modeling concepts discussed above have now become established in the interpretation of SAS data from disordered porous materials [44]. However, a major focus in the present studies was to determine the relative importance of the surface-fractal component as a function of the hydration time and fume additive. It should be recalled that the surface-fractal component can be associated with two surface area values: a smooth surface area S_o for the geometrical boundary between solid and pores, and a rough surface area S_{sf} that takes into account all of the fractal roughness present. The surface-fractal rough surface area S_{sf} could be extracted by extrapolation of the surface-fractal scaling down to the assumed minimum applicable length-scale R_C:

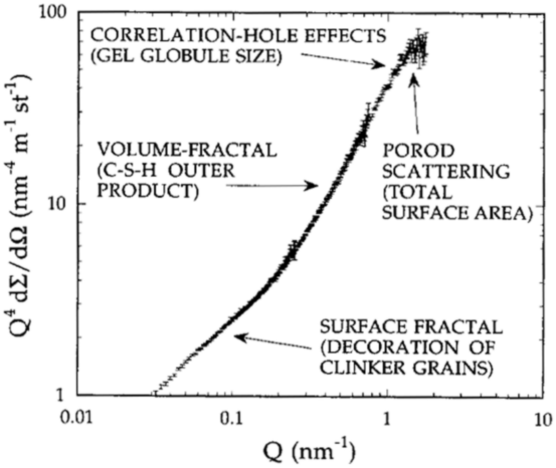

FIGURE 2. SANS data schematic. Circularly averaged, absolute-calibrated $Q^4 d\Sigma/d\Omega$ data vs. Q for hydrated cement (28-day SF/PC with 10% wt cement solids replaced by fume F) showing main features associated with the microstructural model. Incoherent flat-background scattering has been subtracted out. The combined standard uncertainties, computed during data reduction, are shown for each data point.

$$S_{sf} = S_O\left[\frac{\xi_s}{R_C}\right]^{(D_s - 2)} \tag{2}$$

Despite the generally imprecise determination of ξ_s using eq 1 alone, discussed previously, a satisfactory evaluation of S_{sf} results from eq 2, provided that R_C has been deduced from the volume-fractal regime at high Q, and that there exists sufficient SAS data in the true surface-fractal power-law scattering regime: $QR_C \ll 1 \ll Q\xi_s$. In this $Q^{-(6 - D_s)}$ intensity power-law range, the use of eq 2 to substitute for S_o in eq 1 eliminates the dependence, both of the scattering and of S_{sf}, on the imprecisely determined ξ_s. Once determined, the sur-

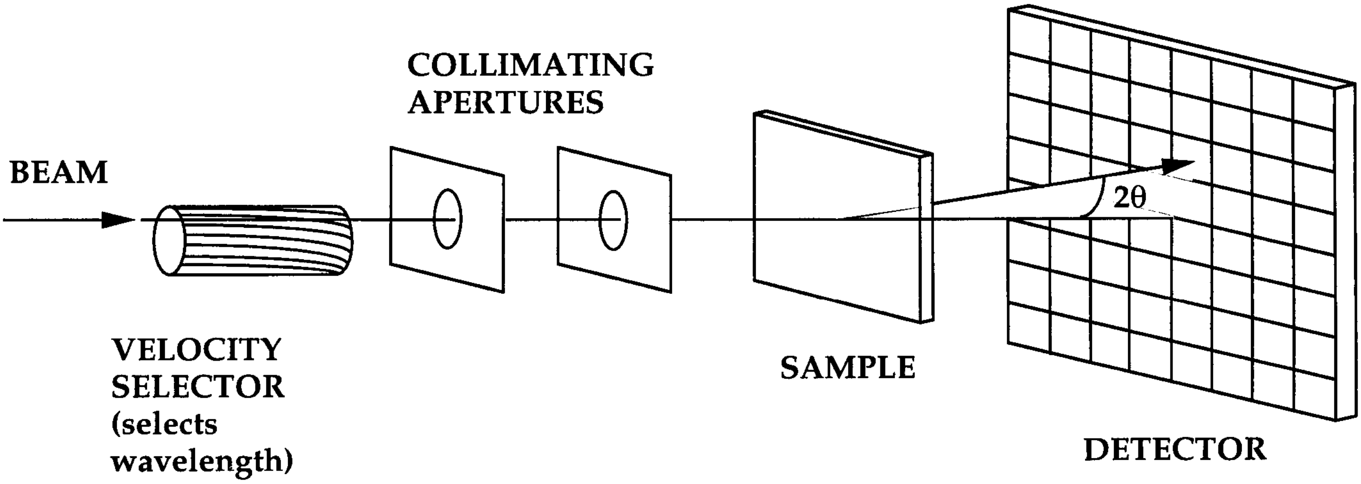

FIGURE 3. SANS experiment schematic.

face-fractal rough surface S_{sf} could be compared with the total surface area per unit sample volume S_T as obtained independently from the Porod scattering law at high Q ($Q > 1.4\ \text{nm}^{-1}$):

$$[\text{Limit as } Q \to \infty]\ \frac{d\Sigma}{d\Omega} = \frac{2\pi|\Delta\rho|^2 S_T}{Q^4} \tag{3}$$

It is assumed that both of the fractal microstructure components are composed of the outer-product C-S-H gel globules, and that this material dominates the total cement surface area per unit sample volume (S_T). The surface areas per unit sample volume within the surface- and volume-fractal components are then, respectively, S_{sf} and $S_{vf} = S_T - S_{sf}$. If, within the C-S-H outer-product groundmass, the relationship between the internal surface area and the C-S-H solid volume fraction is the same for material deposited on clinker grain surfaces (surface-fractal) and for self-standing material in the volume between clinker grains (volume-fractal), then two surface-area ratios become of interest. The ratio S_{sf}/S_T should be a measure of the C-S-H outer-product fraction deposited on the grain surfaces, and the ratio S_{vf}/S_{sf} should be a measure of the ratio of free-standing inter-grain material to that deposited on the clinker grain surfaces. In the studies of SF/PC blends, the fraction S_{sf}/S_T and the ratio S_{vf}/S_{sf} were found to be batch-independent, to be relatively insensitive to uncertainties in some of the model fit parameters (e.g., ξ_s), and to be related to the particle morphologies in the respective fume additives.

Experimental Details

Figure 3 shows the geometry of a typical SANS experiment. The present experiments on hydrating cement systems were carried out at the Center for Neutron Research of the National Institute of Standards and Technology (NIST), Gaithersburg, Maryland [45], using the NIST/Exxon/University of Minnesota/Texaco 30 m SANS instrument. A collimated beam of neutrons of wavelength λ, 0.8 nm and $\Delta\lambda/\lambda$ resolution 10%, was passed through thin, parallel-sided samples of 0.5- to 1-mm thickness enclosed within quartz optical sample cells. The scattered neutrons were registered on the instrument's two-dimensional detector array. The SANS data were corrected for empty beam and background counts, calibrated against a scattering standard, and circularly averaged to give $d\Sigma/d\Omega$. By changing the instrument collimation and the sample-to-detector distance, data were obtained over a Q range of 0.03 to $2.0\ \text{nm}^{-1}$, sufficient to probe length-scales of a few nanometers up to ≈200 nm, directly, and to infer some information on length-scales larger than this.

For the larger length-scales associated with the SF morphology, ultrasmall-angle X-ray scattering (USAXS) studies were carried out using the NIST X23A3 beamline, National Synchrotron Light Source, Brookhaven National Laboratory, Upton, New York. This is a Bonse-Hart double-crystal instrument [46], where, in the present studies, 0.124-nm wavelength (10-keV energy) X-rays and germanium (111) crystal optics were used to provide an ultrahigh SAXS resolution. The experimental design is shown in Figure 4. The scattered X-ray intensity was measured with a photodiode detector as the double-crystal analyzer monolith was rocked away from the straight-through beam diffraction condition. Whereas the USAXS configuration intrinsically is line smeared, the scattering could be geometrically calibrated with respect to the incident beam intensity without the need for a standard scatterer. Knowledge of the precise instrument geometry also made possible an

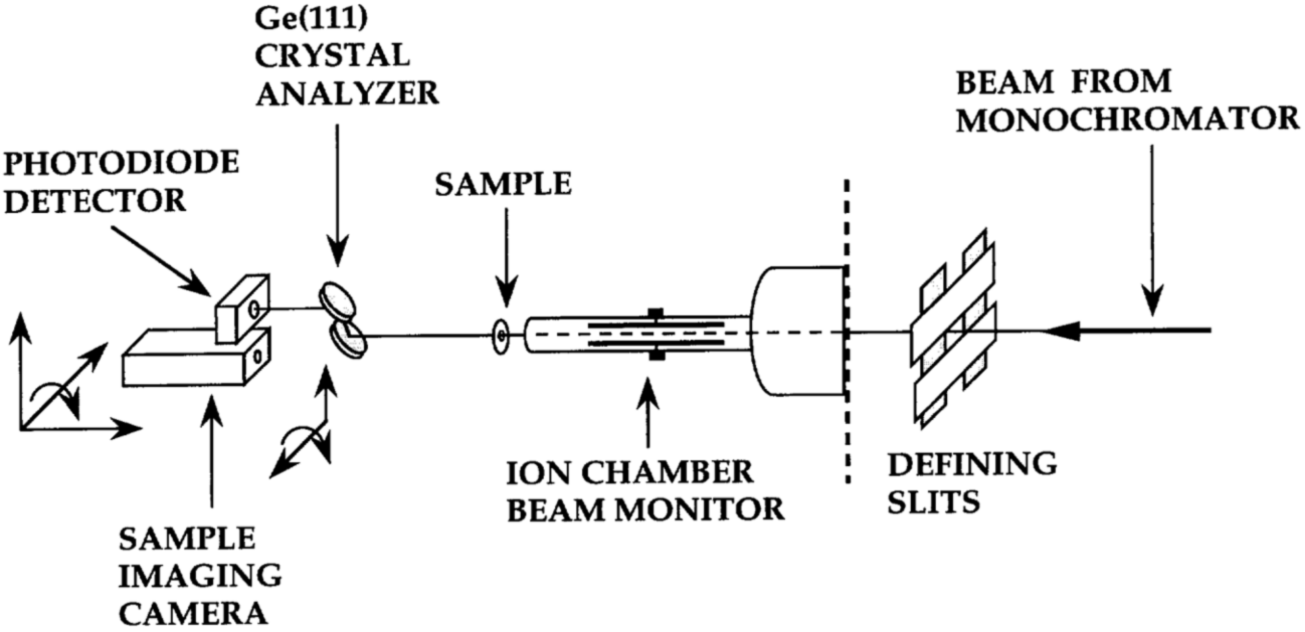

FIGURE 4. USAXS experiment schematic.

accurate desmearing of the data using the well-established algorithm by Lake [47], resulting in desmeared, effectively circularly averaged, absolute-calibrated, SAXS $d\Sigma/d\Omega$ data as a function of Q. The effective Q range was 0.004 to 0.3 nm^{-1}, limited at low Q by the Darwin width [46] of the Ge (111) optics, and at high Q by background effects due to air scattering. Some SANS experiments were carried out to extend the maximum Q achieved and to interrelate the USAXS and SANS data, but the USAXS Q range was sufficient to determine the main SF particle size distributions.

The six SFs studied were designated A, B, C, D, E, and F, obtained from a range of commercial suppliers. For USAXS measurements, all were initially studied as thin (~0.1 mm) powder deposits sandwiched between layers of X-ray compatible tape. In subsequent measurements, fumes B through F were diluted in a water slurry suspension in an approximate 4.0 water/fume weight ratio, whereas fume E was already supplied in slurry form. This weight ratio was the same as the water/fume weight ratio in a 0.4 w/s cement with 10% of the PC weight replaced by fume. Each slurry suspension was placed in a 1-mm-thick water cell with X-ray compatible tape windows. This concentration of fume gave acceptable (10 to 15%) X-ray penetration with negligible multiple scattering. For the SANS measurements, all the fumes were placed as slurry suspensions in 1-mm-thick quartz optical cells.

The 0.4 w/s cement pastes were prepared from three batches of PC powder. The first was used in an earlier study [20] that involved using fume slurry A. The second was used in studies with fumes B, C, D, and E, each hydrated for 3, 7, 14, 28, and 560 days. The third was used with fume F, hydrated for 3, 7, 14, and 28 days. All of these studies used 10% by weight replacement of the PC by SF. In addition, the third powder was used in studies at the same ages with 6% by weight fume replacement, and after 28 days with 20% fume replacement. All of the samples made using the first and third cement powders were mixed and then allowed to hydrate in the 1-mm cells (i.e., all were 1 mm thick). All of the samples using the second powder were hydrated for close to the specified time intervals as 25-mm cubes, then, just prior to the experiment, they were sliced under water to give ~0.5-mm-thick SANS specimens. These slices were stored under lime water until the experiment, and finally sealed wet in the quartz cells.

Results and Discussion

Real-Time Early Hydration

The real-time early hydration of the 0.4 w/s SF/PC blend with fume A has been discussed in detail elsewhere [20,21]. The main effects of the fume addition were the emergence of a greater surface-fractal component in the hydrated cement paste and a more gradual development of both types of fractal structure during the period of the peak hydration rate. However, more total surface area was observed prior to the hydration peak. This is consistent with a reported acceleration in the initial production of C-S-H [48], but may also be due to the high fume surface area.

In presenting these earlier results here, as well as the

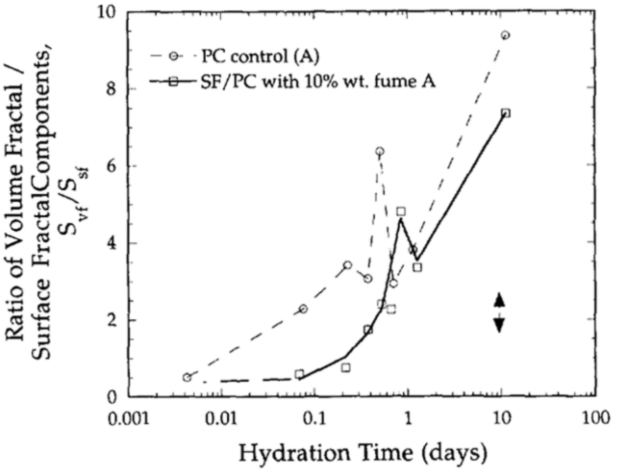

FIGURE 5. Volume-fractal/surface-fractal ratio vs. hydration time for silica fume/Portland cement (SF/PC) with fume A. The 0.4 w/s SF/PC blend with 10% wt solids replacement by silica fume A and 0.4 w/c PC control (A) were both made using PC from the first batch. Unreacted clinker surface is included in the surface-fractal component at early times. The estimated standard uncertainty is given by the double arrow.

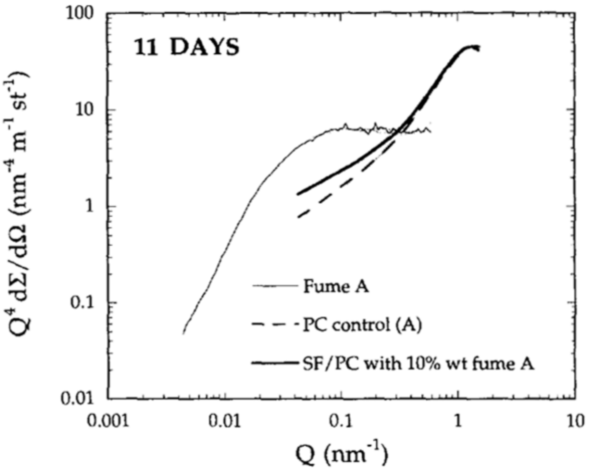

FIGURE 6. $Q^4 d\Sigma/d\Omega$ vs. Q at 11-day hydration for silica fume/Portland cement (SF/PC) with fume A. The 0.4 w/s SF/PC blend with 10% wt solids replacement by silica fume A and 0.4 w/c PC control (A) were both made with PC from the first batch. Fitted curves only are given for the hydrated cements. Combined USAXS data (powder deposit) and SANS data (fume slurry) are shown for fume A, normalized to the fume SANS scattering contrast, and approximately rescaled to the volume fraction of fume actually present in the SF/PC blend.

SANS results discussed below, the microstructural model of eq 1, and the surface-fractal extrapolation of eq 2, were applied to the SANS data to obtain S_{sf}. Meanwhile, the total overall surface area S_T was measured from the Q^{-4} Porod scattering component at $Q > 1.4$ nm^{-1}, by subtracting the incoherent flat-background scattering and fitting eq 3. From S_{sf} and S_T, values of S_{vf}, S_{sf}/S_T, and S_{vf}/S_{sf} could also be obtained.

For the real-time early hydration study, Figure 5 presents a plot of S_{vf}/S_{sf} vs. hydration time for both the SF/PC blend and the PC control. The generally lower value of S_{vf}/S_{sf} for the SF/PC blend is due to the higher value of S_{sf} associated with the greater surface-fractal component in this system. Figure 5 also shows the more gradual evolution towards a final microstructure in the SF/PC blend (not to be confused with the overall degree of hydration). For both pastes, there are peaks in this ratio coincident with the period of the peak hydration rate. The subsequent drop in S_{vf}/S_{sf} (before rising again) suggests a relatively abrupt onset for the emergence of the surface-fractal components in both systems, somewhat delayed with respect to the initial emergence of the volume-fractal components.

The effects of the fume addition are not confined to early hydration times. Figure 5 shows that differences persist to the end of the 11-day hydration period studied. This is confirmed further by Figure 6, where fume SAS data and cement SANS model fits are shown together. Comparison of Figures 5 and 6, with reference to Figure 2, shows that, as hydration progresses, the surface-fractal component in the SF/PC blend remains more prominent than for the PC control.

Level of Fume Addition

The effect of varying the level of fume addition is shown in Figure 7 for 0% (control), 6%, 10%, and (at 28-day hydration only) 20% by weight, cement solids replacement with silica fume F in 0.4 w/s SF/PC paste. The SANS intensity increases across the whole Q range with increasing SF replacement, particularly in the surface-fractal regime at lower Q values.

Figure 8 shows that the total (Porod) surface area S_T is increased significantly by the replacement of some of the cement solids by fume. At 28-day hydration, a 10% weight replacement increases S_T, over the PC control, by 50×10^6 m^{-1}, more than 40%. It is deduced below that the surface area of initially unreacted SF within the 10% SF/PC paste is $\sim 6 \times 10^6$ m^{-1}. Because the scattering contrast for the hydrating SF/PC blends was assumed to be between water and C-S-H, not silica, the apparent contribution to S_T is $\sim 14 \times 10^6$ m^{-1}. However, in the absence of any fume activity, the ~12% volume reduction in cement solids could make the net gain in S_T virtually zero. It is clear that the main mechanism for increasing the surface area by fume addition must be through chemical reaction of the silica to form C-S-H, rather than through the surface area of the unreacted fume itself.

For all the samples studied, Figure 8 shows only a slight increase in S_T over the 25-days hydration following the first ~3 days. (This differs from the case of blast furnace slag additions in PC, where the surface area

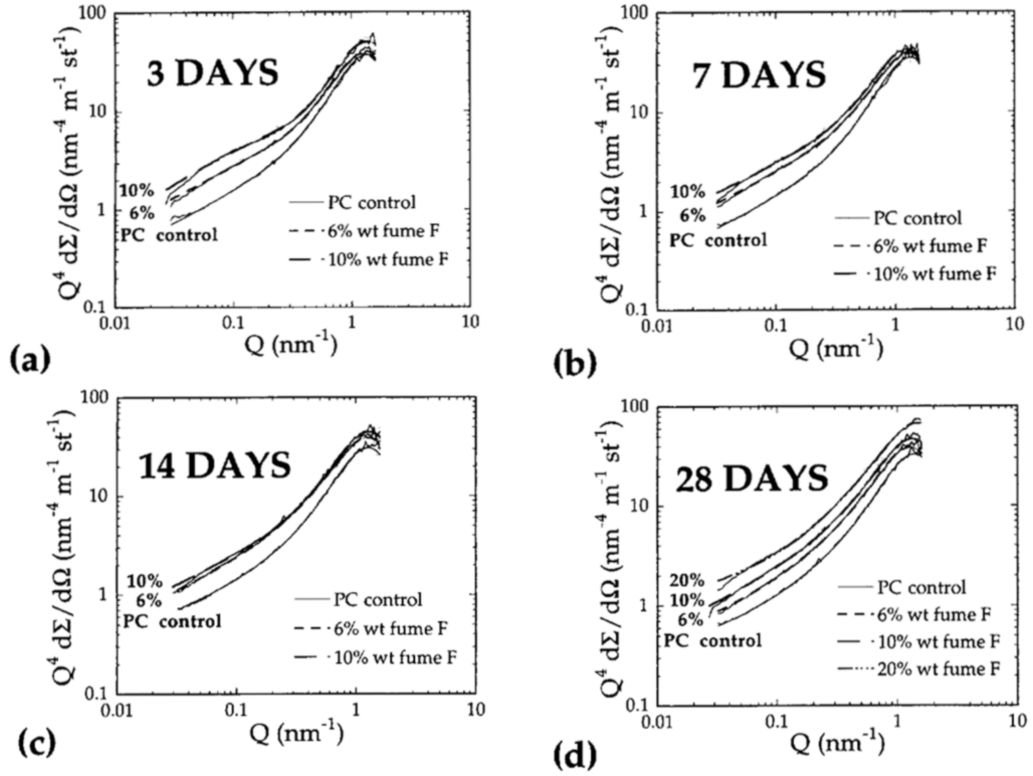

FIGURE 7. $Q^4 d\Sigma/d\Omega$ vs. Q for silica fume/Portland cement (SF/PC) with fume F after hydration for (a) 3, (b) 7, (c) 14, and (d) 28 days. The 0.4 w/s SF/PC blend with 6% 10% and 20% wt. solids replacement by silica fume F, and 0.4 w/c PC control were made using PC from the third batch. Thin lines follow the data and dark lines follow the fits.

was found to increase steadily throughout the first month [15].) Although differences in S_T, for different SF loadings, appear to be largely established within the first 3 days, more significant increases in S_T over longer hydration times (months) are not ruled out.

Figure 8a reveals a minimum in the total surface after 7-days hydration, for each of the samples made using fume F. Similar minima in S_T were observed at various times during the first 28 days for the samples made with fumes B through E, even though, as discussed above, the sample preparation differed between these two sets of samples. In both cases, the temporary reduction in surface area might be attributed to shrinkage effects that reduce the space available to the C-S-H outer-product phase, but more research would be needed to confirm this.

Figure 8b shows that, after 28-day hydration, while S_T increases almost linearly with fume content up to 10%, the linearity does not extend to a 20% fume loading. This implies that a saturation level of fume exists beyond which there is little further increase in pozzolanic reaction, as all of the Ca^{2+} ions are used up. Furthermore, the curve of Figure 8b suggests that there can be only a modest (few percent) increase in the scattering contrast, $|\Delta\rho|^2$, due to a reduction in CH/S molar ratio within C-S-H formed in the presence of SF (e.g., $C_{1.6}SH_{1.9}$, instead of $C_{1.7}SH_{2.1}$). Any larger increase would cause the apparent variation of S_T in Figure 8b to curve upwards.

Whereas the main effect of the fume loading on the total surface area evolution is to increase S_T during the early stages of hydration, a more complex picture emerges when the volume- and surface-fractal components are compared. Figure 9 shows that, for the PC control and the 6% SF/PC blend with fume F, the surface-fractal component, as measured by S_{sf}/S_T, decreases fairly monotonically. Thus, the 6% fume loading has the net effect of increasing the total hydrated surface area relative to the PC control (Figure 8), without significantly changing the volume-fractal dominated microstructure that develops in the absence of fume (Figure 9). This implies an enhanced microstructure, with increased amounts of C-S-H gel binding the cement together, with the surface regions around clinker grains and other particles "bound in" and no more distinguishable topologically than in the microstructure of the PC control.

For the 10% SF/PC blend, the surface-fractal component does not decrease over the 28-day hydration period. Indeed, it shows some increase between 7 and 14 days. Thus, in this case, regions of surface-deposited C-S-H gel close to the surfaces of clinker grains, SF, and

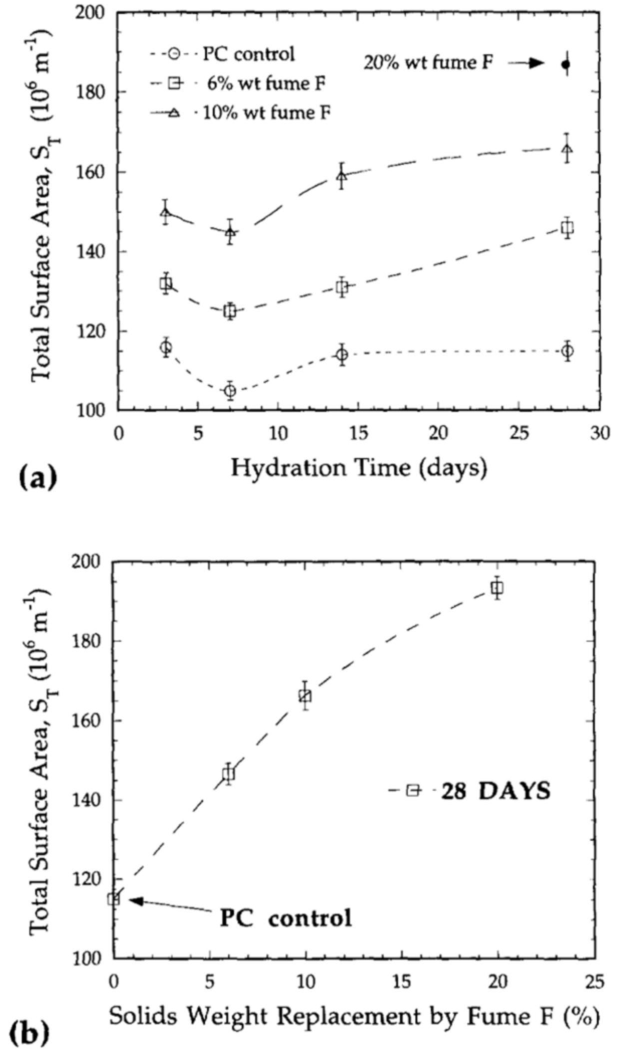

FIGURE 8. Silica fume/Portland cement (SF/PC) with fume F. Total surface area S_T vs. (a) hydration time, and (b) fume content at 28-day hydration. Vertical bars give computed standard uncertainties derived from the Q^{-4} Porod scattering fits measured at $Q > 1.4$ nm^{-1}.

other particles remain distinguishable from the volume-fractal C-S-H gel outer-product, and are not so well bound in to the C-S-H inter-grain microstructure. For the 20% SF/PC blend, the result at 28-day hydration lies between the values for the 6% and 10% fume loadings. This is difficult to interpret without data from earlier times, because it is not known whether S_{sf}/S_T is increasing or decreasing. If increasing, then a complex time-dependence is implied as the fume loading is increased.

Overall, the results suggest that the optimum solid weight replacement by fume F at a 0.4 w/s ratio lies between 6% and 10%. Other work [49] tends to confirm that the optimum enhancement of many of the properties of SF/PC blends typically occurs in this range of fume loading for hydration at ambient temperatures.

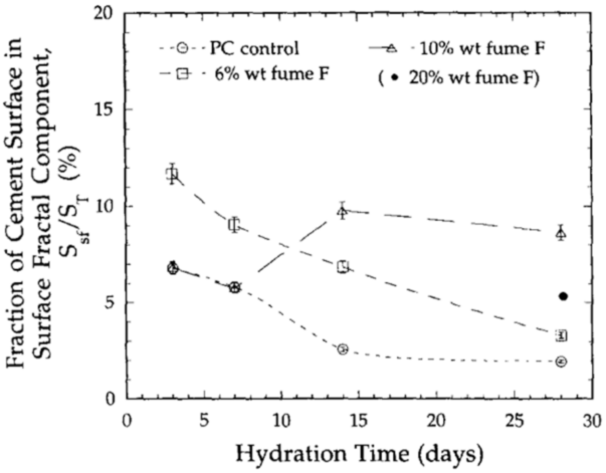

FIGURE 9. Relative surface-fractal component vs. hydration time for silica fume/Portland cement (SF/PC) with fume F: 0.4 w/s SF/PC blend with 6% 10%, and 20% wt solids replacement by silica fume F, and 0.4 w/c PC control. Vertical bars give estimated uncertainties.

USAXS and SANS Characterization of Silica Fume Slurries

Figure 10 presents the combined absolute-calibrated USAXS and SANS $d\Sigma/d\Omega$ data vs. Q for the SF slurries B through F. Unlike the SANS data for the hydrating cement blends, which show distinct fractal power-law forms, the fume SAS curves are mainly characteristic of broad discrete particle size distributions [23]. The curves are also virtually indistinguishable from each

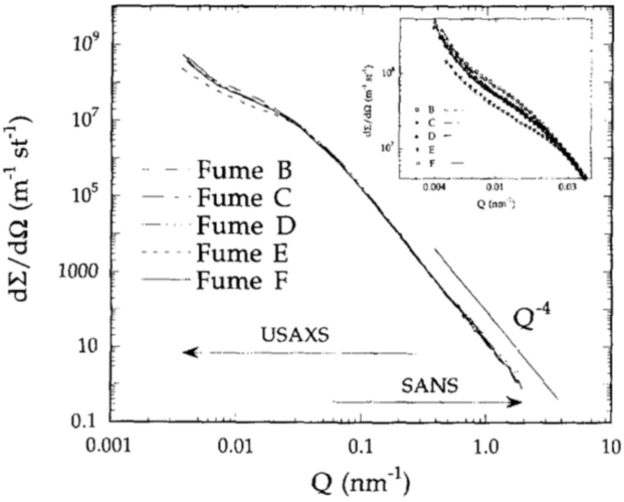

FIGURE 10. Absolute-valibrated $d\Sigma/d\Omega$ vs. Q for silica fume slurries B through F. Combined desmeared USAXS and circularly averaged SANS data with USAXS data normalized to the SANS calibration. The lines are provided to guide the eye in the main plot, whereas the inset shows the low-Q data with the scattering predicted for the maximum entropy size distributions.

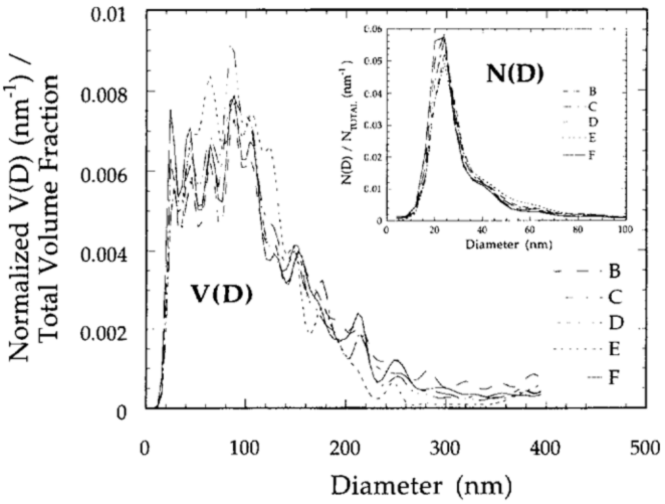

FIGURE 11. Silica Fume Slurry Particle Size Distributions. The volume-fraction size distributions, V(D), versus particle diameter, D, have been obtained from the SAS data using MaxEnt methods. The inset shows the derived number-density size distributions, N(D). V(D) and N(D) have been normalized to unit integral values to compare different fumes.

other at $Q > 0.04$ nm^{-1}. Below this Q, shown more clearly in the inset, differences are discernible among the fumes, with an upturn in the scattering associated with coarse features. The Porod scattering, which dominates the scattering for $Q > 0.1$ nm^{-1}, yields surface areas of $\sim 14 \times 10^6$ m^{-1} for all of the fume slurries. Because, as discussed below, the average solid silica volume fraction within each slurry was ~16%, the specific surface areas of the solid fumes were deduced to be ~ 40,000 m^2 kg^{-1}, an acceptable value for reasonably well-dispersed SFs [49]. These numbers allow estimates to be made of the unreacted fume surface area contributions in the SF/PC pastes. In the 10% SF/PC blends, the fume volume fraction in each sample was ~6%, giving an initial sample surface area contribution of $\sim 6 \times 10^6$ m^{-1}, with values approximately scaling with the fume weight loading in other samples.

The scattering particle size distributions, which give rise to the observed combined USAXS/SANS data for fume slurries B through F, were obtained using the entropy maximization method, MaxEnt [50,51]. The MaxEnt method seeks that volume fraction size distribution V(D), which maximizes the configurational entropy with respect to the particle diameter D. Figure 11 presents the V(D) distributions in fractional form. Apart from minor spurious oscillations, the different fumes demonstrate near equivalence. The volume-weighted mean particle diameters lie in the range from 100 to 120 nm for all of the fumes. The absolute V(D) distributions show only minor variations, attributable to uncertainties in the exact slurry concentrations studied, and the absolute total volume fractions average to ~ 16%. The fractional number size distributions N(D) derived from the V(D) distributions are shown in the Figure 11 inset. These show even greater similarity than do the V(D) distributions and are approximately lognormal in shape with modal diameters of 20 to 25 nm. The surface areas calculated from the average diameters of the size distributions are consistent with those determined independently from the Porod scattering and are consistent with the expected characteristics of reasonably well-dispersed fumes [49].

The most significant differences between the fume slurries are at the lowest Q values measured, Figure 10 (inset), where the predicted MaxEnt scattering curves are shown with the data. The additional (upward curving) scattering is predicted by MaxEnt to be the Porod scattering associated with additional volume fractions of coarse features, not included in the size distributions shown in Figure 11. These Porod components were estimated directly from the scattering at low Q, and the associated surfaces from coarse features were deduced as fractions of the total surface (as measured from the main Porod range at high Q). These surface fractions, attributable to coarse features, were used as the differentiating characteristic of fumes B through F, and were estimated as 0.75% for B, 0.55% for C, 0.85% for D, 0.30% for E, and 0.70% for F.

The coarse surface components in the fumes could be attributed either to additional volume fractions of independent coarse particles or, more likely, to low density agglomerates of the particles already characterized in the MaxEnt size distributions. The particles within the agglomerates could not be close packed, because, if this were so, strong interference effects would appear in the SAS curves of Figure 10 [23]. However, these SAS curves are slightly suggestive of those obtained in nanocrystalline-particle consolidation studies where agglomeration is present [52]. Furthermore, TEM studies in general [53], and some preliminary laser scattering particle size analyses of these particular fumes [54], indicate that the SF particles flocculate into large (several μm diameter) loose assemblages, which, nevertheless, cannot easily be broken up by sonic agitation.

Of the fumes B, C, D, and F, supplied as powders, it was known [55] that the fabrication route of fume D resulted in the most silica particle agglomeration, as well as the inclusion of many oversized impurity particles. Fume E, supplied as a slurry, was a more expensive processed form of fume D, especially purified and dispersed with colloids to reduce both agglomeration and the number of oversized impurities. It is of interest that the estimated coarse surface components for fumes D and E were, respectively, the most and the least among fumes B through F, whereas the coarse

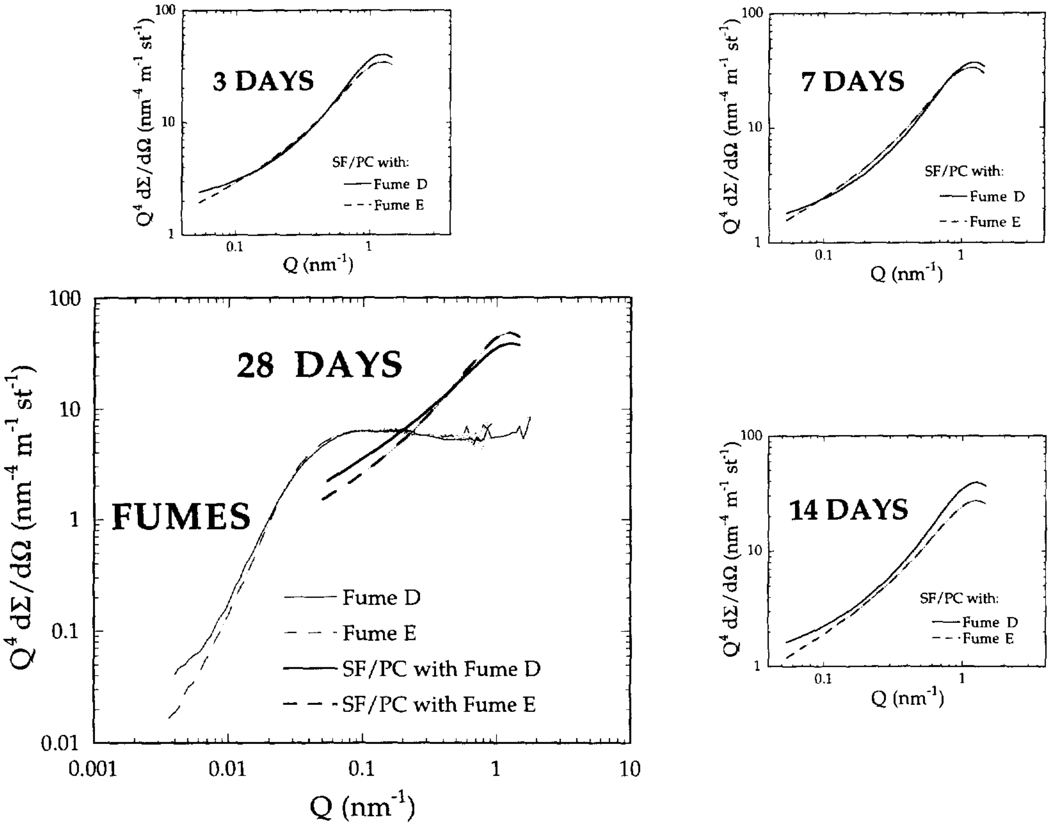

FIGURE 12. $Q^4 d\Sigma/d\Omega$ vs. Q for silica fume/Portland cement (SF/PC) blends with fumes D and E after hydration for 3, 7, 14, and 28 days. The 0.4 w/s SF/PC blend with 10% wt solids replacement by silica fumes D and E, were made using PC from the second batch. Fitted curves only are given for the hydrated cements. At 28-day hydration, combined USAXS and SANS data for the fume slurries are also shown, normalized to the SANS scattering contrast and rescaled to the volume fractions of fume actually present in the SF/PC blends.

surface components for B, C, and F were intermediate between those for D and E.

Effects of Different Silica Fume Additives on Hydration

In Figure 12, the SAS data for fume D, with the most coarse surface component, and for fume E, with the least coarse surface, are compared with the SANS data for their associated SF/PC blends, as hydration progresses in the cements. The differences in the fume slurries are reflected in differences in the SANS from the hydrating cement blends. These differences undergo a complex evolution, but they persist through the 28-day hydration time. The microstructural effects of the different fumes B through F were quantified using eqs 1 through 3. Figure 13 shows the development of the ratio S_{vf}/S_{sf} through the first 28 days. Whereas at up to 14 days, the highest ratio occurs for the SF/PC blend containing the highest coarse fume surface component, this trend has reversed by 28 days. This pattern of reversal suggests two competing processes, one favoring the development of S_{sf} and the other S_{vf}. However, there are not enough data points in time to fit parameter models. These different time-dependences probably are linked to independent observations [48] that SF first reacts with the Ca^{2+} ions produced in the normal cement hydration reactions to form more C-S-H, but later can react with C-S-H itself to produce a modified form of C-S-H. Other microscopy studies [56] also suggest that long-term reorganizations of the C-S-H gel take place at extended hydration times.

The differences in the microstructural evolution among the SF/PC blends persist to long hydration times, as shown in Figure 14a at 560-day hydration. By this time, the correlation of a high S_{vf}/S_{sf} ratio with a low coarse fume surface component is well established, as is shown in Figure 14b for the SF/PC blends using fumes B through E. Unfortunately, no data were available for a PC control sample at this age, but Figure 13 strongly suggests that the S_{vf}/S_{sf} ratio would reach, or exceed, that for the SF/PC blend with fume E.

Figures 12 through 14 should be considered in relation to our earlier discussion of the amount of fume added in SF/PC blends, especially with reference to

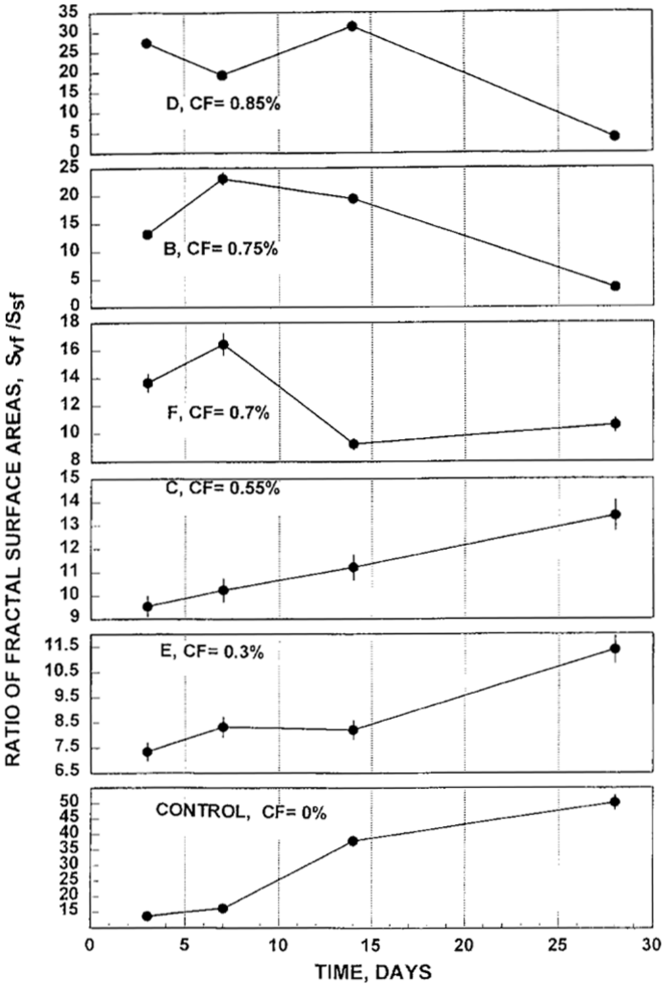

FIGURE 13. Volume-fractal/surface-fractal ratio vs. hydration time for silica fume/Portland cement (SF/PC) blends with fumes B through F. CF = coarse fume surface component. Vertical bars give estimated standard uncertainties.

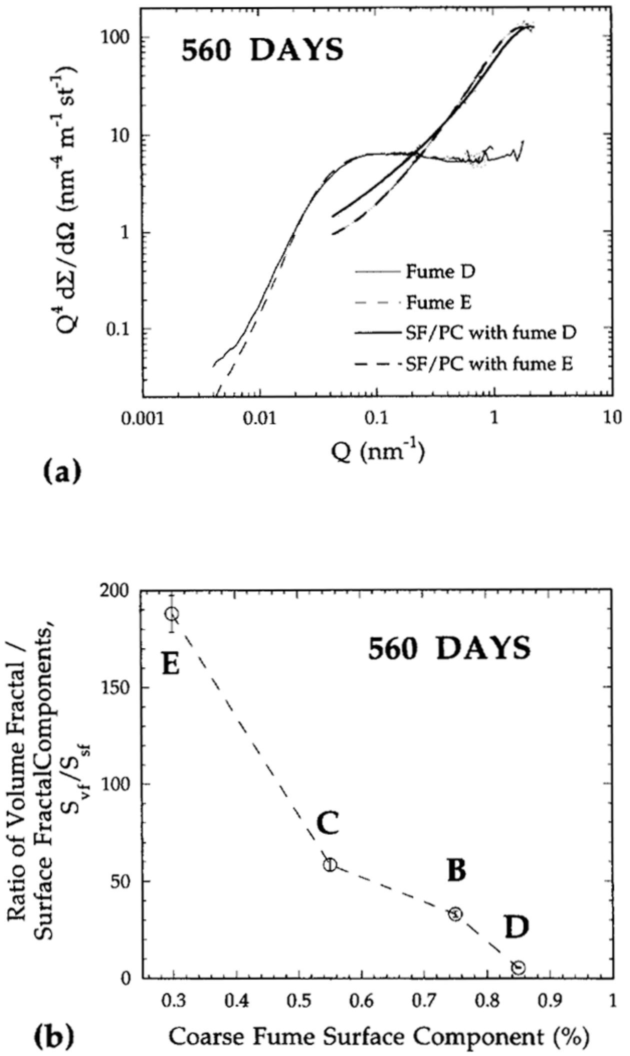

FIGURE 14. Effects of hydration for 560 days on silica fume/Portland cement (SF/PC) blends with fumes B through D. (a) $Q^4 d\Sigma/d\Omega$ vs. Q as in Figure 12. (b) Volume-fractal/surface-fractal ratio vs. coarse fume surface component.

Figure 9. At early hydration times (up to ~ 14 days), either a lower SF loading or a lower coarse fume surface component gives rise to a higher fraction of surface in the surface-fractal component and, correspondingly, a lower S_{vf}/S_{sf} ratio. At later hydration times, this situation reverses.

If the coarse fume surface component is solely due to a few oversized particles, it is difficult to understand how variations in this fraction account for all of the microstructural changes observed during hydration. The time-dependences of the microstructural parameters are more likely related to the degree that SF particles are initially present as loose assemblages between the clinker grains, rather than as dispersed fine particles more easily bound in to the C-S-H microstructure. As Figure 1 suggests, individual SF particles can be deposited on the clinker grain surfaces or enveloped in the evolving C-S-H gel outer-product structure during early hydration. However, if some of the particles already measured in the size distributions of Figure 11 organize into large, diffuse, but stable assemblies of connected particles, then these are likely to reside out in the inter-grain pore space, and deny some of this volume to C-S-H gel formation until a much more extended hydration time has elapsed.

The parameter S_{vf}/S_{sf} is a distinguishing characteristic of the paste microstructure. As yet, no tests have been done relating this to the macroscopic properties of concrete such as strength. Consequently, it is not known what an acceptable value of this ratio should be. However, physical reasoning suggests that a higher value is preferable in mature cement, and this has been linked with a lower coarse fume surface component. Thus, among fumes B through F, E should provide the most effective fume additive, and D the least effective.

Concluding Discussion

The SAS studies of early cement hydration, of the effects of the level of fume replacement, and of the effects of different fume additives, lead to a number of important conclusions. Foremost among these is that the major factor responsible for increasing the total surface area (S_T) in a hydrating SF/PC blend, over that in a pure PC, is the chemical reaction of SF with the PC hydration products to produce an enhanced level of C-S-H gel outer-product. Conversely, the relatively high surface area of the fume itself has only a secondary effect. Moreover, up to a solids replacement level of 10% by weight, the amount of additional gel is linearly related to the added SF but, beyond 10%, the effect levels off.

Another set of important conclusions arises from the use of fractal parameters to characterize the nature of the C-S-H gel. The fraction of the total surface that is in the surface-fractal component (S_{sf}/S_T) is generally greatest at early times. However, the detailed time-dependence of this fraction varies nonlinearly with SF level. This nonlinear dependence suggests that two competing processes are involved, one affecting S_T, and the other S_{sf}/S_T.

As hydration progresses, the total surface area and the fraction of surface within the surface-fractal component can be compared to evaluate the developing microstructure within SF-enriched cement blends. For a mature SF/PC blended cement to have optimally enhanced strength and durability properties, a high overall surface area (S_T) of binding C-S-H outer-product is desirable, without the persistence of a large, physically distinct, surface-fractal component around the clinker grains. The optimal SF replacement level for achieving this, using a typical fume, seems to lie in the 6 to 10% range.

A second fractal ratio, the ratio of surface area within the volume-fractal component to that in the surface-fractal (S_{vf}/S_{sf}), also provides some insight into the C-S-H gel/SF relationship. The time-dependence of the ratio can be used to distinguish the effects of different SFs in the hydration of SF/PC blends. Among the fumes themselves, the major difference observed is in the fraction of coarse (>1 μm) agglomerates. A direct connection has been made between the existence of these coarse agglomerates in the SF and possible deleterious microstructure development in the hydrating SF/PC cement pastes. On the other hand, unreacted SF particle agglomerates remain potentially active, and the extended time-dependence might prove useful in developing tailor-made SF/PC blends, whose properties (e.g., strength development) evolve, in certain environments, in a controlled way with extended hydration time. Thus, the processing of SF to adjust the level of agglomerates might provide a means to achieve specific performance levels.

Finally, SANS and SAXS provide unique capabilities for investigating the microstructural modifications produced by additives such as SF. This is due to their ability to measure, nondestructively, the representative microstructures over the large range of fine length-scales required to quantify fractal systems.

Acknowledgments

We thank Professor D.L. Gress, of the Department of Civil Engineering, University of New Hampshire, for preparation of the cement samples incorporating fumes B through E, and for invaluable discussions concerning the characteristics of these fumes. L-S.H. Lum of NIST's Ceramics Division is thanked for useful discussions, and for a preliminary characterization of fumes B through F by laser scattering particle size analysis.

References

1. Hjorth, L. *Philos. Trans. R. Soc. Lond. Ser. A* **1983,** *310,* 167–173.
2. Mehta, P.K.; Gjorv, O.E. *Cem. Concr. Res.* **1982,** *12,* 587–595.
3. Chatterji, S.; Thaulow, N.; Christensen, P. *Cem. Concr. Res.* **1982,** *12,* 781–784.
4. Xi, Y.; Jennings, H.M. In *Materials Science of Concrete III;* Skalny, J.P.; Mindess, S., Eds; American Ceramic Society: Westerville, OH, 1992; pp 37–69.
5. Pratt, P.L. *Mater. Res. Symp. Proc.* **1986,** *85,* 145–156.
6. Jenning, H.M.; Bhatty, J.I.; Hodson, S.K. In *Advances in Cementitious Materials;* Mindess, S., Ed; American Ceramic Society: Westerville, OH, 1991; pp 289–318.
7. Smith, D.M.; Hua, D.-W.; Earl, W.L. *MRS Bull.* **1994,** *XIX-4,* 44–48.
8. Allen, A.J.; Windsor, C.G.; Rainey, V.S.; Pearson, D.; Double, D.D.; Alford, N.M. *J. Phys. D* **1982,** *15,* 1817–1833.
9. Pearson, D.; Allen, A.J.; Windsor, C.G.; Alford, N.M.; Double, D.D. *J. Mater. Sci.* **1983,** *18,* 430–438.
10. Allen, A.J.; Pearson, D. In *Microstructural Characterization of Materials by Non-Microscopic Techniques;* Anderson, N.H.; Jenson, D.J.; Eldrup, M.; Hansen, N.; Leffers, T.; Lilholt, H.; Pedersen, O.B.; Singh, B.N., Eds; Riso National Laboratory: Rosskilde, Denmark, 1984; pp 175–180.
11. Pearson, D.; Allen, A.J. *J. Mater. Sci.* **1985,** *20,* 303–315.
12. Pearson, D.; Allen, A.J.; Sambell, R.A.J. *Small-Angle Scattering Data on Cements with Pozzolanic Additives;* Harwell Report AERE-R11609; HMSO: London, England, 1985.
13. Allen, A.J.; Schofield, P. In *Scaling Phenomena in Disordered Systems;* Pynn, R.; Skjeltorp, A., Eds; Plenum Publishing Co.: London, England, 1985; pp 189–195.
14. Allen, A.J.; Schofield, P. In *Neutron Scattering Data Analysis;* Johnson, M.W., Ed; Institute of Physics: London, England, 1986; pp 97–102.
15. Allen, A.J.; Oberthur, R.C.; Pearson, D.; Schofield, P.; Wilding, C.R. *Philos. Mag. B* **1987,** *56,* 263–288.
16. Allen, A.J.; Baston, A.H.; Wilding, C.R. *Mater. Res. Symp. Proc.* **1989,** *137,* 119–125.
17. Allen, A.J. *J. Appl. Cryst.* **1991,** *24,* 624–634.
18. Allen, A.J.; Baston, A.H.; Bourke, P.J.; Jefferies, N.L. *Small-Angle Neutron Scattering Studies of Diffusion and*

Permeation through Pores in Clays; Harwell Report AERE-R13261; HMSO: London, England, 1988.

19. Allen, A.J.; Baston, A.H.; Bourke, P.J.; Jefferies, N.L. In *Water-Rock Interactions VI;* Miles, D.L., Ed; Balkema: Rotterdam, Holland, 1989; pp 9–13.
20. Allen, A.J.; Livingston, R.A. In *Proc. 5th CANMET/ACI Int. Conf. on Fly Ash, Silica Fume, Slag and Natural Pozzolans in Concrete;* Malhotra, V.M., Ed; American Concrete Institute: Detroit, MI, 1995; pp 1179–1200.
21. Livingston, R.A.; Neumann, D.A.; Allen A.J.; Rush, J.J. *Mater. Res. Soc. Symp. Proc.* **1995,** *376*, 459–469.
22. Livingston, R.A.; Allen, A.J. In *Proc. 8th CIMTEC World Ceramics Congress and Forum on New Materials, Vol. A: Ceramics in Architecture;* Vincenzini, P., Ed; CIMTEC: Faenza, Italy, 1995; pp 573–580.
23. Porod, G. In *Small-Angle X-ray Scattering;* Glatter, O.; Krattky, O., Eds; Academic Press: London, England, 1982; pp 17–51.
24. Taylor, H.F.W. *Cement Chemistry;* Academic Press: London, England, 1990; pp 123–166.
25. Sears, J. *Neutron News* **1992,** *3.3*, 29–37.
26. Thomas, J.J.; Jennings, H.M.; Allen, A.J. *Adv. Cem. Based Mater.* **1998,** *7*, 119–122.
27. Aldridge, L.P.; Bertram, W.K.; Sabine, T.M.; Bukowski, J.; Young, J.F.; Heenan, R.K. *Mater. Res. Soc. Symp. Proc.* **1995,** *376*, 471–479.
28. Winslow, D.N.; Bukowski, J.M.; Young, J.F. *Cem. Concr. Res.* **1994,** *24*, 1025–1032.
29. Berliner, R.; Heuser, B.J.; Popovici, M. *Mater. Res. Soc. Symp. Proc.* **1995,** *376*, 481–486.
30. Haussler, F.; Eichhorn, F.; Baumbach, H. *Cem. Concr. Res.* **1994,** *24*, 514–526.
31. Eichorn, F.; Haussler, F.; Baumbach, H. *J. Physique IV* **1993,** *3*, 369–372.
32. Haussler, F.; Hempel, M.; Eichhorn, F.; Hempel, A.; Baumbach, H. *Physica Scripta* **1995,** *T57*, 184–189.
33. Castano, V.M.; Schmidt, P.W.; Hornis, H.G. *J. Mater. Res.* **1990,** *5*, 1281–1284.
34. Vollet, D.; Craievich, A.; Regourd, M. *J. Am. Ceram. Soc.* **1984,** *67*, 315–318.
35. Winslow, D.N. *Cem. Concr. Res.* **1985,** *15*, 817–824.
36. Winslow, D.N.; Bukowski, J.M.; Young, J.F. *Cem. Concr. Res.* **1995,** *25*, 147–156.
37. Beddoe, R.E.; Lang, K. *Cem. Concr. Res.* **1994,** *24*, 605–612.
38. Kriechbaum, M.; Degovics, G.; Laggner, P.; Tritthart, J. *Adv. Cem. Res.* **1994,** *6*, 93–101.
39. Groves, G.W. *Mater. Forum* **1990,** *14*, 1–8.
40. Lange, D.A.; Jennings, H.M.; Shah, S.P.; Quenard, D.A. *Ceram. Trans.* **1992,** *16*, 347–363.
41. Meakin, P. *Phys. Rev. A* **1983,** *27*, 1495–1507.
42. Viehland, D.; Li, J.-F.; Yuan, L.-J.; Xu, Z. *J. Am. Ceram. Soc.* **1996,** *79*, 1731–1744.
43. Roess, L.C.; Shull, C.G. *J. Appl. Phys.* **1947,** *18*, 308–313.
44. Bale, H.D.; Schmidt, P.W. *Phys. Rev. Lett.* **1984,** *53*, 596–599.
45. Hammouda, B.; Krueger, S.; Glinka, C.J. *J. Res. Natl. Inst. Stand. Tech.* **1993,** *98*, 31–46.
46. Long, G.G.; Jemian, P.R.; Weertman, J.R.; Black, D.R.; Burdette, H.E.; Spal, R.D. *J. Appl. Cryst.* **1991,** *24*, 30–37.
47. Lake, J.A. *Acta Cryst.* **1967,** *23*, 191–194.
48. Wu, Z-Q.; Young, J.F. *J. Mater. Sci.* **1984,** *19*, 3477–3486.
49. Malhotra, V.M.; Carette, G.G.; Sivasundaram, V. In *Advances in Concrete Technology;* Malhotra, V.M., Ed; CANMET: Ottawa, Canada, 1992, pp 925–991.
50. Potton, J.A.; Daniel, G.J.; Rainford, B.D. *J. Appl. Cryst.* **1988,** *21*, 663–668.
51. Jemian, P.R.; Allen, A.J. *J. Appl. Cryst.* **1994,** *27*, 693–702.
52. Allen, A.J.; Krueger, S.; Skandan, G.; Long, G.G.; Hahn, H.; Kerch H.M.; Parker, J.C.; Ali, M.N. *J. Am. Ceram. Soc.* **1996,** *79*, 1201–1212.
53. Sinclair, W.; Groves, G.W. *J. Mater. Sci. Lett.* **1986,** *5*, 101–102.
54. Lum, L.-S. Personal Communication, NIST, Gaithersburg, MD, 1997.
55. Gress, D.L. Personal Communication, University of New Hampshire, Durham, NH, 1997.
56. Sarkar, S.L. *Microscope* **1990,** *38*, 141–152.